Research Article

Omid Sartipzadeh, Seyed Morteza Naghib*, Farhad Shokati, Mehdi Rahmanian*, Keivan Majidzadeh-A, Yasser Zare, and Kyong Yop Rhee*

Microfluidic-assisted synthesis and modelling of monodispersed magnetic nanocomposites for biomedical applications

https://doi.org/10.1515/ntrev-2020-0097
received October 24, 2020; accepted November 19, 2020

Abstract: Droplet microfluidic was devoted to design and fabricate robust devices in the field of biosensing, tissue engineering, drug delivery, cell encapsulation, cell isolation, and lab-on-a-chip. Chitosan was widely used for different biomedical applications because of its unique characteristics such as antibacterial bioactivities, immune-enhancing influences, and anticancer bioactivities. In this research, a model is used for investigating the formation and size of composite droplets in a microfluidic device. The role of the velocity flow ratio in the composite droplet characteristics such as the generation rate and composite droplet size is described. According to the results, a desirable protocol is developed to control the properties of the composite droplets and to compare the size and rate of the composite droplets in a micro device. Furthermore, the level set laminar two-phase flow approach is exploited for studying the composite droplet-breaking procedure. An experimental procedure is used for validation of the simulation process. Various sizes and geometries of the composite droplets are fabricated to depict a potential in biomedical applications such as bioimaging, biosensing, tissue engineering, drug delivery, cell encapsulation, cancer cell isolation, and lab-on-a-chip.

Keywords: microfluidic device, nanocomposite droplet, cell isolation, tumour modelling, experimental validation, lab-on-a-chip

1 Introduction

Recently, nanoparticles/nanomaterials have fascinated abundant curiosity in various fields of engineering and technology [1–26]. Cytocompatibility and biocompatibility are critical issues in biomedical applications of materials and nanostructures [27–32]. Preparation of biocompatible polymeric micro/nanoparticle systems has attracted much attention for diagnosis in biosensing [33], cell encapsulation in tissue engineering, and drug loading in controlled release [27,34–36]. Chitosan (CS) and its derivatives are cytocompatible biopolymers that have shown excellent potentials in biomedical applications including controlled release and targeted delivery [37–39]. Owing to the unique CS characteristics, depicting pH-sensitivity, it is typically applied to tumour therapy as an anticancer drug delivery vehicle [40,41]. A controlled release with a suitable profile via CS-based containers is very important because it can depict a broad variety of smart stimuli-sensitive responses according to the variations in the circumambient physiological environments [9]. Several methods have been developed for the synthesis of CS micro/nanoparticles such as ionic gelation, emulsification, coacervation, reverse micellar, and spray drying; however, they have a critical drawback of heterogeneous particles size distribution [37].

Droplet microfluidic has facilitated an extensive range of recent applications including high-throughput screening, diagnostics [42,43], digital polymerase chain reaction [44,45],

* **Corresponding author: Seyed Morteza Naghib,** Nanotechnology Department, School of Advanced Technologies, Iran University of Science and Technology, Tehran, Iran, e-mail: naghib@iust.ac.ir
* **Corresponding author: Mehdi Rahmanian,** Biomaterials and Tissue Engineering Research Group, Department of Interdisciplinary Technologies, Breast Cancer Research Center, Motamed Cancer Institute, ACECR, Tehran, Iran, e-mail: mrahmanian1@gmail.com
* **Corresponding author: Kyong Yop Rhee,** Department of Mechanical Engineering, College of Engineering, Kyung Hee University, Yongin, 446-701, Republic of Korea, e-mail: rheeky@khu.ac.kr
Omid Sartipzadeh: Nanotechnology Department, School of Advanced Technologies, Iran University of Science and Technology, Tehran, Iran
Farhad Shokati, Keivan Majidzadeh-A, Yasser Zare: Biomaterials and Tissue Engineering Research Group, Department of Interdisciplinary Technologies, Breast Cancer Research Center, Motamed Cancer Institute, ACECR, Tehran, Iran

efficient screening of antibiotics delivery [46,47], biosensing [48–50], imaging [51,52], and tissue engineering [53,54]. The ability of microfluidic-based systems for particular treatment and transportation of a slight amount of liquids has established the theme as robust platforms for fabricating advanced micro/nanocarriers in drug delivery [55]. Production of a repeatable drug release profile needs synthesizing a monodisperse drug micro/nano-container, which might not be sufficient with routine synthesis approaches [56]. Moreover, conventional methods are unable to synthesize micro/nanocarriers for controlling the delivery of some drugs, proteins, and growth factors and possessed various release profiles, where a rigorous control above the formulation of the used micro/nanocarriers is needed [55]. Controllability and consistency of the tuneable profile of cargo release are important subjects in the productive applications of micro/nanocarriers, which rely on the formulation, configuration, and conformation such as their shape, uniformity, size, and composition [57]. Microfluidic-assisted systems have been used for preparing the formulated drug micro/nanocarriers devoted to successful therapeutic feedback. Microfluidic-assisted techniques allow the generation of monodisperse, multicomponent, and multi-functional drug micro/nanocarriers with favourably controllable chemical, physical, and biological characteristics to enhance the efficiency of cargo transport, release, distribution, and elimination in the treatment progress [58]. Furthermore, these systems are effectual for designing and fabricating drug micro/nanocarriers possessed programmed, on-demand, and tuneable release profile. Incorporating the microfluidic techniques and micro-engineered chip into a suitable device for controlled drug release applications in a chip or fabricating the drug micro/nanocarriers with promising organ-on-a-chip platforms permits cost-efficient investigations on the effectiveness of different drug delivery systems. Finally, these promising microengineered systems can probably accomplish the break between the *in vitro* and *in vivo* studies [55]. Therefore, it seems there is a critical need for predicting the size and shape of particles in the microfluidic-assisted devices that should be addressed. Consequently, a numerical study was conducted to predict and control the size of CS microparticles that could be used in various biomedical applications.

In this work, we studied the effects of the velocity flow ratio on the generation rate and size of composite droplets. The COMSOL Multiphysics® 5.4 simulation software was exploited for this purpose. Operating microfluidic devices were expanded in an amended way that yielded oil-composite-oil double emulsions. We described the role of physical properties of two immiscible liquids and flow rate ratios on the composite droplet geometries including size, shape, volume, length, formation, and velocity of droplets.

2 Approach

The approach used here is established according to the evaluation of the computer simulation outcomes and comparison with the experimental results. The scale and production rate of a droplet is affected by the microfluidics flow-focusing device (MFFD) geometry [27] and the flow rate ratio of both phases [28]. Here, we investigated the chemical and physical properties of the composite (magnetite nanoparticle [MNP] and CS) including (1) MNP weight percentage, (2) CS concentration, and finally (3) CS and oil volumetric flow ratio. The schematic representation of the MFFD structure is illustrated in Figure 1 and the complete dimensions are presented in Table 1. As seen, the device used in this study contains the orifice, one outlet, and three inlets.

3 Modelling and experimental

3.1 Simulation process

The simulation process of this study is detailed in supporting information. Towards the simulation, the 2D plane was used to represent the device. The free triangular mesh was decided at a step of 0.5 µm. A total of 17,83,821 domain elements and 8,979 boundary elements were implemented for the model. The CS/MNPs-OA composite and vegetable oil were used for the fluid characteristics from COMSOL Multiphysics®, and they were applied as the dispersed phase and continuous phase,

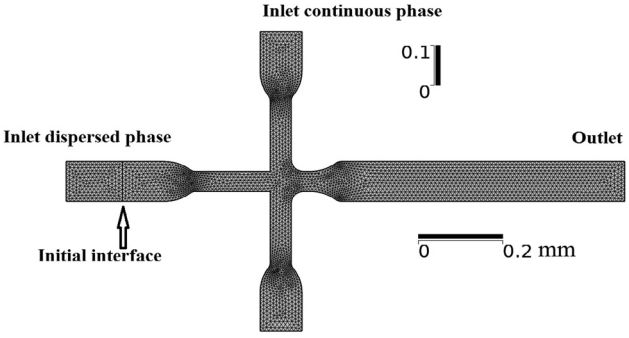

Figure 1: Schematic representation of the MFFD exploited in the simulation processes: 2D model of the defined boundary conditions and meshes for the composite droplet production.

Table 1: Detailed dimensions of MFFD

Property	Inlet length (μm)	Outlet length (μm)	Inlet width (μm)	Outlet width (μm)	Angle (degree)
Dispersed phase	280	180	100	50	90
Continuous phase	100	180	100	50	
Orifice	50	80	50	100	40
Outlet	—	670	100	100	0

respectively. The compositions were demonstrated as incompressible Newtonian liquids, and the duct walls were characterized as a wetted wall situation with a constant contact angle for all the cases. The properties of the chosen substances are summarized in Table 2. The schematic graph of MFFD and the boundaries established as inlet and outlet channels for continuous and dispersed phases are illustrated in Figure 1.

3.2 Modelling and experimental

The materials used in this research were ferrous chloride tetrahydrate ($FeCl_2{\cdot}4H_2O$, 98% [w/w]), ferric chloride hexahydrate [$FeCl_3{\cdot}6H_2O$, 98% (w/w)], aqueous ammonia solution [NH_3, 25% (v/v)], aqueous tetramethylammonium hydroxide solution [$(CH_3)_4N(OH)$, 25% (v/v)], oleic acid [$C_{18}H_{34}O_2$, 99% (v/v)], ethanol [EtOH, 96% (v/v)], acetic acid glacial [$C_2H_4O_2$, 100% (v/v)], aqueous glutaraldehyde solution [$C_5H_8O_2$, 50% (w/v)], sorbitan monooleate [non-ionic surfactant, span®80], vegetable oil [corn oil, pure], and the low molecular weight CS [deacetylation degree 90%, 170 kDa] from Sigma-Aldrich.

The MFFD was sketched using SolidWorks® 2019 software. Then, the mold was fabricated by the standard replica molding soft-lithography technique. A thick photoresist film (SU-8, Microchem, MA, USA) spun on a silicon wafer at 500 rpm for 10 s and repeated at 2,500 rpm for 30 s to produce the mold of MFFD. The coated layer on the silicon wafer was baked at 65°C for 5 min and at 95°C for 10 min, and the wafer was immersed in a solvent to remove unexposed zones of photoresist.

The polydimethylsiloxane (PDMS) casting procedure was exploited for constructing the MFFD. Mold surfaces must be accurately rinsed with isopropanol and acetone in several steps before casting to assure clean surface without residues and particles. The PDMS gel was used to prepare an elastomer and a curing agent (SYLGARD 184, Dow Corning Corporation, Midland, MI, USA) mixture with a 10:1 ratio. The molding gel was poured into the cast and placed in a shaker for 1 h or until all the air bubbles come out. Then, the mold was kept in an oven at 75°C for 4 h to cure PDMS [59].

The bonding process of the microfluidics mold was established in several steps. The process was described in supporting information. The schematic representation of the microfluidic chip manufacturing process and the fabricated MFFD is shown in Figure 2a and b, respectively.

MNPs were synthesized by the method described by Berger *et al.* [29]. The reaction stoichiometry is important. The aqueous ammonia reacts with Fe^{2+} and Fe^{3+} ions to produce magnetite, Fe_3O_4, as presented in equation (1).

$$2FeCL_3 + FeCL_2 + 8NH_3 + 4H_2O{\cdot}\ Fe_3O_4 + 8NH_4CL. \quad (1)$$

To achieve the highest conversion yield, the mole ratio of iron(III) to iron(II) solutions in the reaction must be equal to 2 [29]. The solutions were poured and mixed at high speed. An aqueous NH_3 was added dropwise by the burette into the beaker. It should be noted that the addition rate of ammonia into the beaker is decisive, and a burette is a suitable instrument for slowing the addition rate. The black sediment of magnetite was formed quickly. Then, the sediment was settled for 20 min. In the following, the remaining liquid was decanted and disposed of the liquid and centrifuged. The sludge-like solid at the bottom of

Table 2: Fluid properties used in this simulation

Property	Density (kg/m^3)	Dynamics viscosity (mPa s)	Contact angle (rad)	Surface tension (mN/m)
Vegetable oil	920.29	38.50	—	—
1% CS + MNPs	1169.4	16.5615	0.44312	50.502
0.5% CS + MNPs	1159.3	7.314	0.40177	49.916
0.2% CS + MNPs	1155.2	2.0425	0.38961	48.878

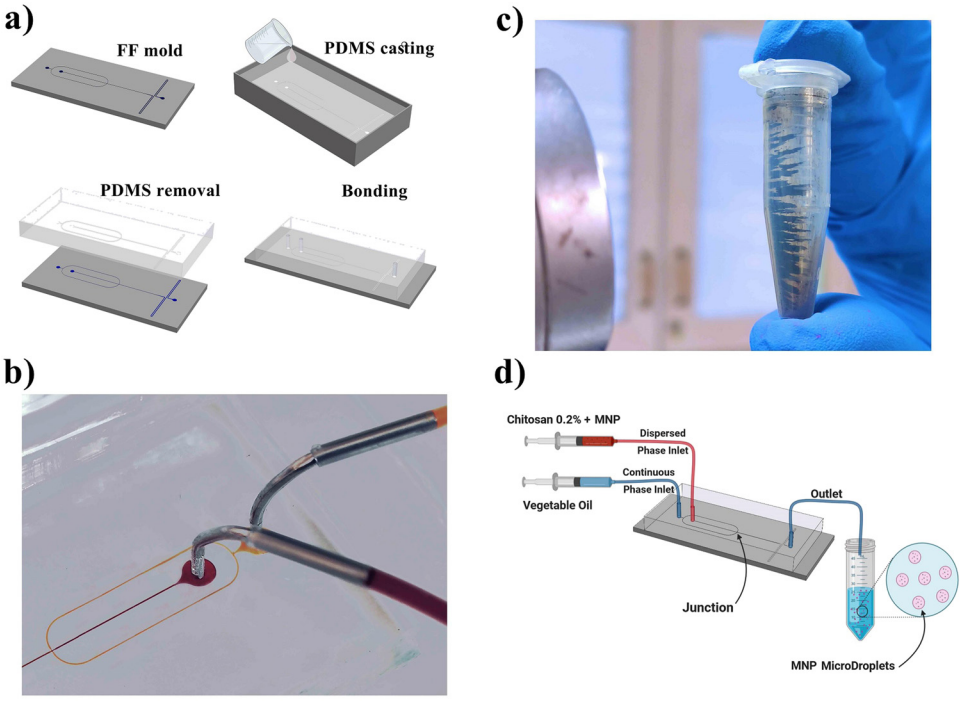

Figure 2: Design and fabrication of MFFD: (a) solid work schematic of the manufacturing process of MFFD; (b) microscopic image of MFFD with inlets, outlet, and junction; (c) synthesized MNP (Fe_3O_4); (d) schematic illustration of the microfluidic setup for producing MNP/CS nanocomposite droplet.

the microtubes was magnetite. To remove the remaining ammonia, 25% tetramethylammonium hydroxide was added and stirred with a thin glass rod until the sludge was completely suspended in the liquid. The contents of the tubes were poured into a vacuum filtration flask with a magnetic stirring bar. Finally, after exhausting the residues from the vacuum filtration flask and placing the material in an oven, the MNP powder was obtained as shown in Figure 2c.

4 Results and discussion

4.1 Simulation results

The pattern of MFFD included the inlet and outlet ducts for dispersed and immiscible liquid flow. The two immiscible liquids were then forced to move via a thin orifice placed in the intersection of vegetable oil and one composite inlet. The shear tension and the pressure of the stream caused by a viscosity enforce the inner liquid to move into a narrow throat. Eventually, the liquid stream cut out inside or downstream of the throat and break up the droplets. Gladwell *et al.* in 2012 investigated the slope of pressure amongst the flow string that the drag at the extra jointing distorted the droplet within the downstream side up to the transcend and the surface stress that a droplet was created [30]. Therefore, the discrete phase stream converted to a slimline stream and break up into droplets. The spread phase plug streams downstream to move on the main conduit, whereas the flow tip of the separated phase congregates to the inlet of the junction, and these steps are reiterated. The droplet production process is classified into three fundamental sections such as (a) squeezing, (b) dripping, and (c) jetting that have been proposed by Mensch *et al.* in 2008 [31]. The squeezing and dripping methods generally occur in microchannel flows around the growth of the droplet, affected by the duct walls' physical confinement. In the squeezing method, the pressure force of the upstream flow applies the main impact upon droplet forming. On the contrary, the capillary number amount is very small to impress it, which can be ignored [29]. In the dripping method, the stress balance between interfacial and viscous driving force is an effect on the scale of the droplet. The droplets break up at an intersection where a couple of inlet conduits of continuous flow are located on both sides of the channel of the dispersed flow and perpendicular to it. The perpendicular inlet channels carry the vegetable oil (continuous flow), and the direct channel is the inlet for the composite (dispersed flow). These two

immiscible streams run into the cross junction of the inlet of the channels. The mechanism of droplet production can be separated into four stages: (I) lag stage, (II) filling stage, (III) necking stage, and (IV) detachment. In the first stage, the liquid stream of the composite penetrates to the throat positioned at the entry of the central conduit. Then, the droplet begins to grow. In the following, the stream flow rate and pressure gradient caused the droplet to move towards downstream of the central conduit [32]. The ComSol Multiphysics software allows access to any of the dynamic and static variables of the MFFD. The production mechanism of the composite droplet by scrutiny and the pressure gradient towards the time can be observed in the stable liquid stream immediately downstream of the inlet of the central conduit. In Figure 3, the series of pictures illustrate different composite droplets production as a function of time (0.2, 0.5, and 1% [w/v]), respectively.

Pressure oscillations in the entry of the central conduit were demonstrated by the place of P point as the time of the production of the composite stream and the detachment step of composite droplets shown in Figure 4a. It displays that the pressure gradient of CS streamline gets up moderately till the droplet starts to be produced under pressure, and the stress force of shear is created and then decreased till the break-up. Next, the quantity and pressure of the composite are still increasing at the P point that is starting to rise. In the following, the formation of the second composite droplet at the P point and the liquid pressure of composite diminished slowly. Regularly, in the process of each droplet generation, the initial pressure is raised and decreased in the end. Furthermore, the inner pressure of the composite droplet is more than that of the circumambient vegetable oil.

Likewise, the dynamic behaviour of the pressure gradient at the place of P point was compared in three ratios of the composite (0.2, 0.5, and 1% [w/v]) as shown in Figure 4b. The velocities of the composites and vegetable oil streamline were adjusted at 3.3 and 11.1 mm/s, respectively. Each of these curves in Figure 4b shows that the pressure fluctuations value is the function of the composite ratio. As the composite ratios increase, the initial pressure of the composite streamlines decreases from 2,000 Pa to 56, 225, and 511 Pa (for 0.2, 0.5, and 1.0% [w/v] of composite ratios). There is a significant pressure drop in the composite streamline (97.2, 88.75, and 74.45%). Increasing the ratio of the composite caused an increasing number of pressure fluctuations per unit time, which reflects the effect of viscosity of the dispersed phase in the continuous phase.

As stated by previous investigations, the quantities of droplets are mainly determined by equilibrium among shearing force and interfacial tension [60]. The proportion of stress force of viscous to interfacial tension is called the capillary number (C_a) applied to represent forces equilibrium [61].

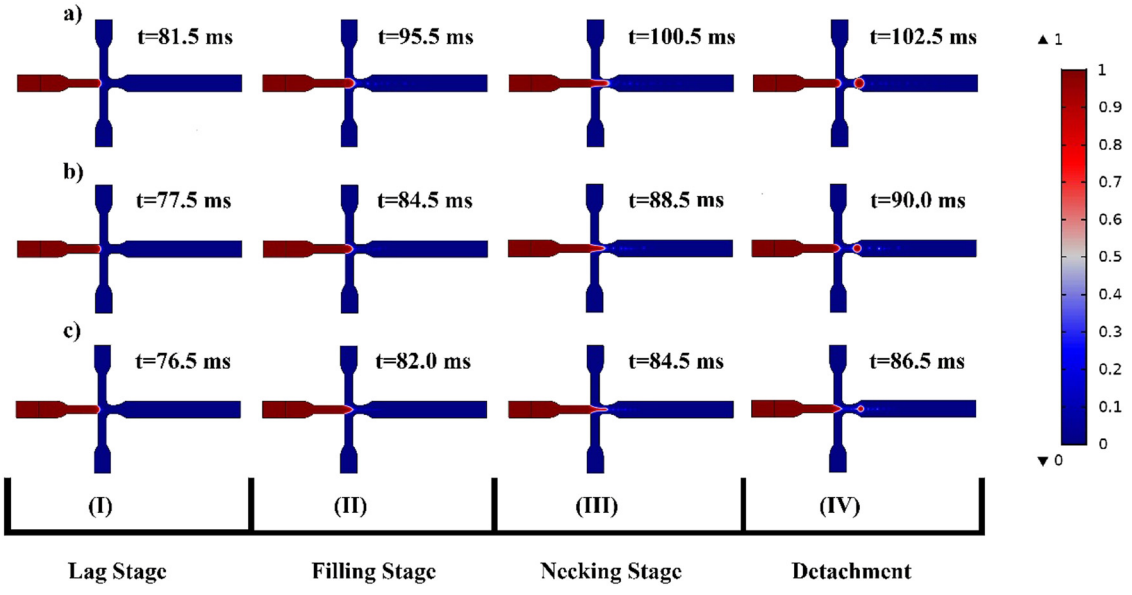

Figure 3: Burst photos of two-dimensional MFFD, pending the implementation of computer simulations of the creation mechanism of composite droplets in micro-conduit. The composite velocity (V_{CS}) is 3.3 mm/s, and the vegetable oil velocity (Vegetable oil) is equal to 11.1 mm/s. The composite ratios are: (a) 0.2%, (b) 0.5%, and (c) 1.0% (w/v).

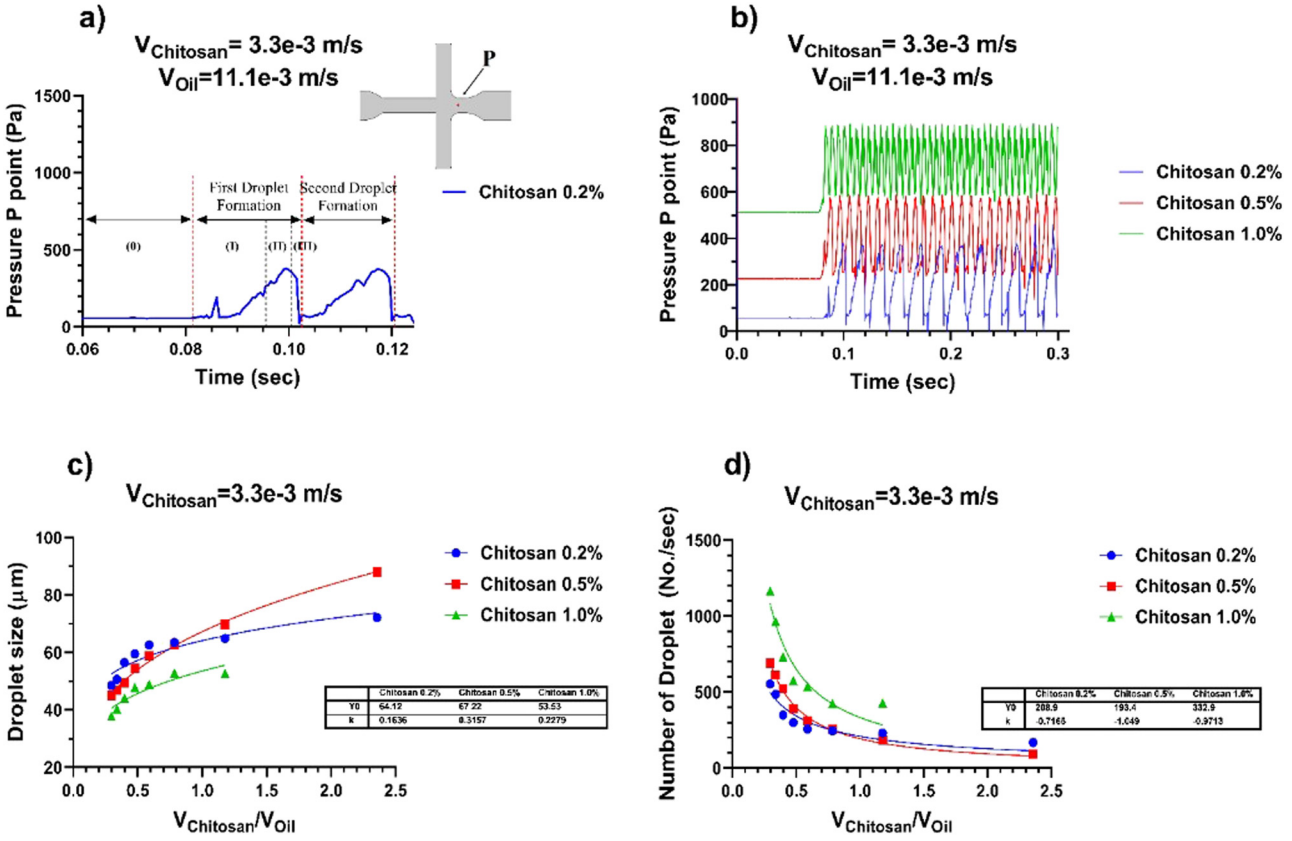

Figure 4: (a) Dynamic pressure behaviour on the place of P point at the time of droplet creation. The P point defines the point placed at the main conduit entry and indicates the evolvement of the droplet making mechanism. Droplet production process: (I) lag stage, (II) filling stage, and (III) necking stage. (b) The software simulation outcomes to the pressure of the composite streamline as a function of time at the place of P point for three ratios of the composite (0.2%, 0.5%, and 1.0% [w/v]). (c) and (d) Influences of velocity and ratios of the composite upon diameter and number of droplet creation per unit time. The velocity of vegetable oil is changed in the range of 1.4–11.1 mm/s, and the composite velocity is adjusted at 3.3 mm/s.

The capillary number is shown as follows:

$$C_a = \frac{\mu_C u_C}{\sigma} = \frac{\mu_C F_C}{s\sigma}, \tag{2}$$

where μ_C and μ_C are the dynamic viscosity and velocity of the continuous phase (mm/s and Pa s), F_C is a continuous liquid rate (µL/s), s is the microchannel surface area (mm^2), and σ is the liquid surface tension (mN/m). The reduced surface tension (σ) leads to a smaller scale of droplets and higher generation repetition. The increase in the composite ratio caused raising the surface tension strongly adapted with the software simulation outcome.

Generally, the Reynolds number at the slight value of Reynolds is applied to qualify liquid flow in MFD. The limited Reynolds number is calculated as:

$$\mathrm{Re} = \frac{\rho u l}{\mu}, \tag{3}$$

where u, ρ, and μ are for velocity, density, and the dynamic viscosity of the liquid, and D is the hydraulic diameter of the duct. For the Reynolds number fewer than 1 ($\mathrm{Re} \ll 1$), the liquid is overcome by viscous stress force. In contradiction to this, the inertial pressure gradient effects are neglected. Therefore, the streamline of liquid particles can be identified precisely [30].

In the next step of software simulation, the generation rate and diameter of the droplet were investigated by variation of the flow rate ratio of composite/vegetable oil and the composite viscosity. Initially, we adjusted the velocity of the composite (V_{CS}) at 3.3 mm/s, and also the vegetable oil velocity ($V_{\text{Vegetable oil}}$) was variable in the range of 1.4–11.1 mm/s. The flow rates ratio of both inlet streams ($\varphi = V_{CS}/V_{\text{Vegetable oil}}$) was obtained between 0.3 and 2.36. The influence of the composite ratios for applying the liquid velocity ratios on the generation rate and diameter of droplets is illustrated in Figure 4c and d. The droplets diameter obtained for three ratios are in a comparable trend, declining this tends to rise with a velocity of vegetable oil. The 0.2% composite of CS/MNPs-OA almost generates the droplets in the range of

50–70 µm, and for 0.5% composite, the diameter is between 45 and 90 µm. However, for the 1.0% composite, this range is only between 40 and 50 µm, which is the lowest value. The velocity of the composite, droplet diameter, and generation frequency is applied as the benchmark to describe the yield of created droplets.

The creation speed of the droplet is considered as a semi-steady flow wherever the input velocity ratio of both flows is constant. Thus, the droplet frequency is calculated from the following equation:

$$f_{\text{droplet}} = \frac{Q_{\text{d}}}{D_{\text{droplet}}}. \tag{4}$$

In addition to this, the number of droplets creation per unit time can be calculated as shown in the following equation [62,63]:

$$\text{No}_{\text{droplet}} = f_{\text{droplet}} \frac{N_{\text{frame}}}{F}, \tag{5}$$

where N_{frame} and F are the total numbers and the rate of each frame. Figure 4d represents the effects of the vegetable oil velocity upon the number of droplets created at the set of the composite velocity for different ratios of the composite (0.2, 0.5, and 1.0% [w/v]).

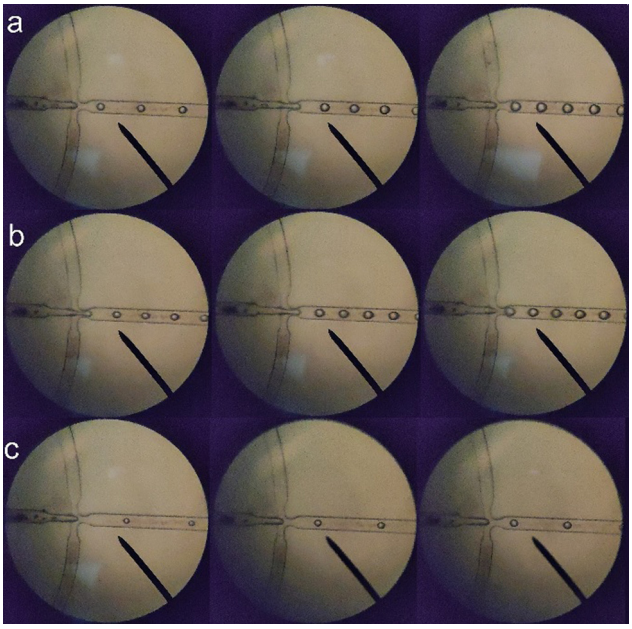

Figure 5: Illustration of the experimental results of the microgel droplet. The velocity of the CS/MNPs-OA composite is fixed at 3.3 mm/s and the vegetable oil velocity is selected 11.1, 5.6, and 1.4 mm/s for 0.2% CS and 0.5%, CS 2.8 mm/s for 1.0% CS. (a) 0.2% CS with 0.5% MNPs-OA. (b) 0.5% CS with 0.5% MNPs-OA. (c) 1.0% CS with 0.5% MNPs-OA.

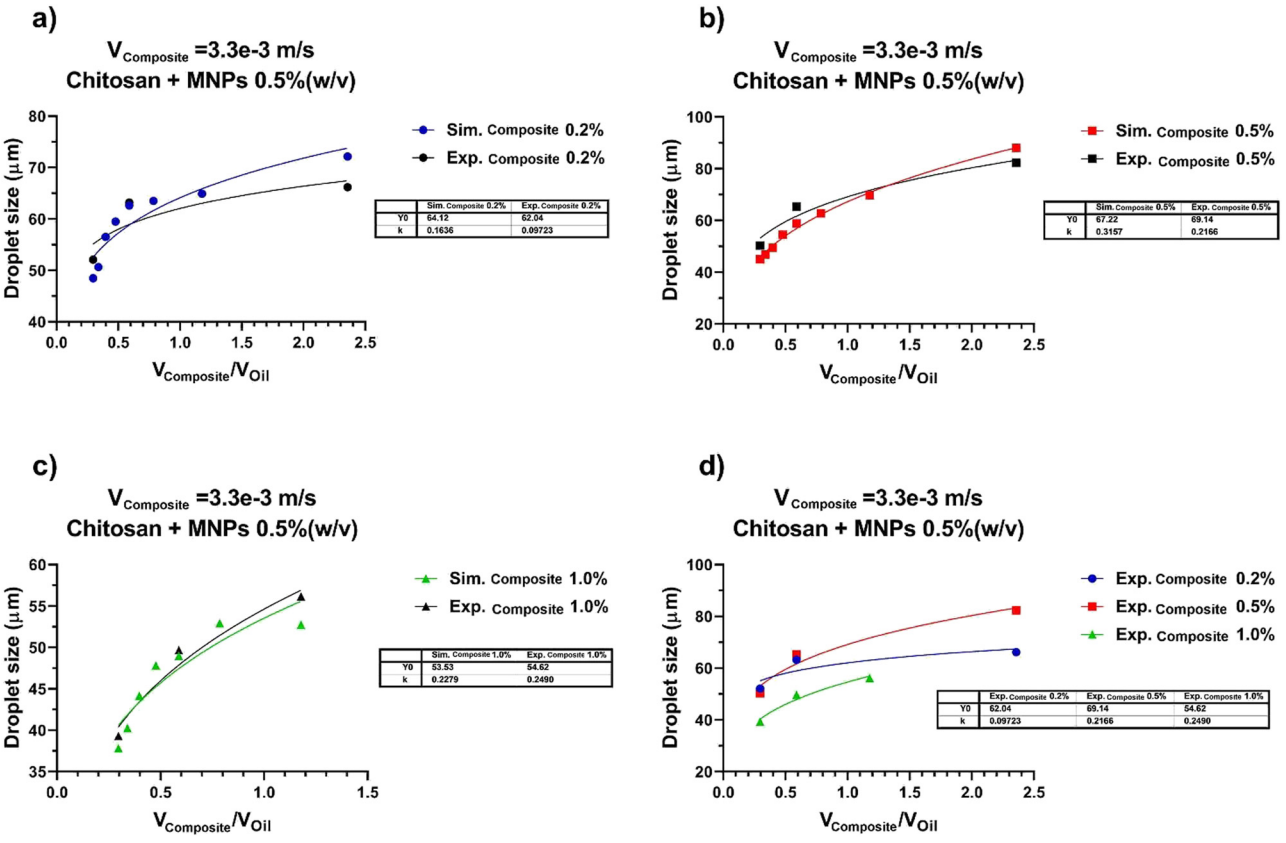

Figure 6: Comparisons of the microgel droplet size of the simulation and experimental results. (a) 0.2% CS; (b) 0.5% CS; (c) 1.0% CS; (d) the effect of the CS concentration on the microgel droplet size.

The vegetable oil velocity may affect the droplet number per unit time. It can be concluded from equations (4) and (5) that the diameters of the composite droplets have a dependence on its creation speed per unit time. In other words, by raising the droplet diameter in a velocity ratio of both liquids, the creation speed of the droplet reduces as shown in Figure 4d. Likewise, the number of composite droplets for three ratios is in a like trend, diminishing this tends to get up with the velocity ratio. It is clear that for 0.2 and 0.5% composites, the creation rate of the droplet is lower than that of 1.0% composite. For the 0.2% composite, the number of droplets per unit time from 230 to 553 can be almost created. In addition, the number of droplets for the 0.5% composite gets up mildly likes the 0.2% composite from 185 to 690. As already stated, the 1.0% composite had a various growth rate (diameter of the droplet) compared to the 0.2 and 0.5% composites in the varying production speed of the droplet which had the highest production rate than two other ratios (from 429 to 1,165 droplets per unit time).

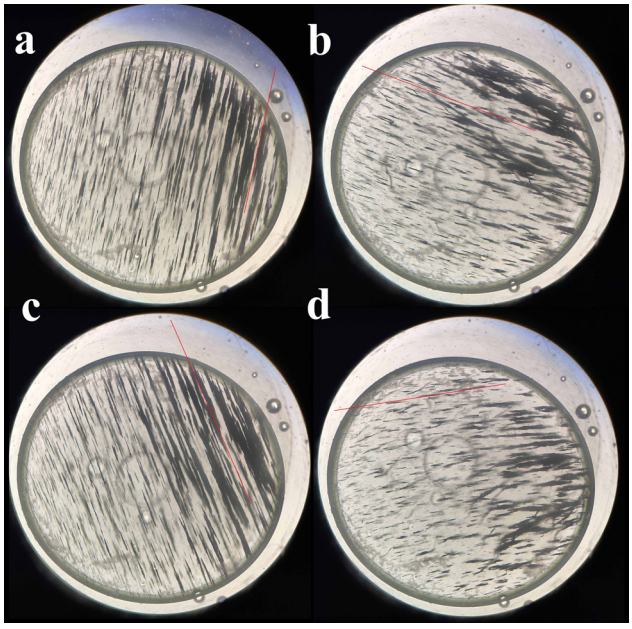

Figure 7: Images of the optical microscope of CS/MNPs-OA microgel droplet (1.0%). The MNPs-OA particles inside the microgel are orientated by applying an external magnetic field (red line). The direction of the external magnetic field is a) slightly inclined to the right, b) slightly inclined to the top, c) slightly inclined to the left and d) slightly inclined to the bottom.

4.2 Experimental results

In the next step of this investigation, the MNPs were dissolved in a solution of oleic acid and ethanol to reduce their oxidation rate and the agglomeration process. The solution of MNPs was prepared by pouring the determined volume ratio of oleic acid in ethanol (volume ratio 1:4) at 70°C and stirred with a mechanical stirrer for 1 h. Then, the MNPs were cleaned with 20% ethanol solution and distilled water twice. As a result, the MNPs-OA was made. CS solutions (0.2, 0.5, and 1.0% w/v) were prepared by dissolving the powder of CS in 100 mL of aqueous acetic acid solution (2%, v/v) in three different beakers at room temperature and left overnight on a magnetic stirrer to obtain a pale-yellow viscous CS solution.

CS solutions were filtered with a syringe filter to remove any undissolved substance. The MNPs-OA were added to three different beakers of CS solutions (0.2, 0.5, and 1.0% w/v) to obtain the solutions with 0.5 wt% of MNPs-OA. All the beakers were stirred for 1 h at room temperature to achieve a homogeneous mixture of CS and MNPs-OA. All the equipment required for the microfluidic chip put together to obtain a microgel of CS/MNPs-OA as shown in Figure 2d. Two syringe pumps were applied to inject the solution of 0.5% CS/MNPs-OA composite and vegetable oil into the MFFD. The velocity rates of CS/MNPs-OA composite and vegetable oil are chosen based on optimal software results. The velocity of CS/MNPs-OA composite was adjusted at 3.3 mm/s, and also the velocity of vegetable oil was selected in the amounts of 11.1, 5.6, and 1.4 mm/s, respectively. Figure 5 represents the microgel droplets size of three different CS/MNPs-OA solutions at the fixed velocity and three different velocities of vegetable oil. In addition, Figure 6 compares the experimental results of 0.2, 0.5, and 1.0% CS/MNPs-OA composites with the software results. As can be seen in the 1.0% CS/MNPs-OA composite, the diameter of the microgel was decreased compared to those synthesized based on the other two concentrations, which were because of its viscosity. This effect of viscosity on the droplet size is shown in Figure 5d. Figure 7 presents a close-up of a CS-MNPS-OA microgel droplet. By changing the spatial position of the external magnetic field applied to the microgel, the nanoparticles in the microgel were oriented in the direction of the applied external field (red line).

5 Conclusions

Reining the geometries of composite droplets in a microfluidic-assisted device is significant because of the nature of the phases present in the material. Control of the shape

and size in a composite system can address many challenges in biomedical applications such as bioimaging, biosensing, 3D cultures, cell encapsulation, drug/gene delivery, organ on a chip, and tissue engineering. Herein, a simulation study was established to find the best platform. The platform was suitable for forming the composite droplets applied to an extensive range of purposes and investigating the mechanism of droplet formation with controllable size and shape. Moreover, an experimental validation was conducted to validate the simulation results. The device could generate the composite droplets with different geometries, representing that many challenges could be addressed in bio-applications of monodispersed nanocomposite microparticles.

Conflict of interest: The authors declare no conflict of interest regarding the publication of this paper.

References

[1] Zare Y, Rhee KY. A simple model for electrical conductivity of polymer carbon nanotubes nanocomposites assuming the filler properties, interphase dimension, network level, interfacial tension and tunneling distance. Compos Sci Technol. 2018;155:252–60.

[2] Zare Y, Rhee KY. Development of a model for electrical conductivity of polymer/graphene nanocomposites assuming interphase and tunneling regions in conductive networks. Ind Eng Chem Res. 2017;56(32):9107–15.

[3] Zare Y. An approach to study the roles of percolation threshold and interphase in tensile modulus of polymer/clay nanocomposites. J Colloid Interface Sci. 2017;486:249–54.

[4] Zare Y. Modeling the yield strength of polymer nanocomposites based upon nanoparticle agglomeration and polymer–filler interphase. J Colloid Interface Sci. 2016;467:165–9.

[5] Zare Y. Estimation of material and interfacial/interphase properties in clay/polymer nanocomposites by yield strength data. Appl Clay Sci. 2015;115:61–6.

[6] Bayat H, Fasihi M, Zare Y, Rhee KY. An experimental study on one-step and two-step foaming of natural rubber/silica nanocomposites. Nanotechnol Rev. 2020;9(1):427–35.

[7] Behdinan K, Moradi-Dastjerdi R, Safaei B, Qin Z, Chu F, Hui D. Graphene and CNT impact on heat transfer response of nanocomposite cylinders. Nanotechnol Rev. 2020;9(1):41–52.

[8] Jiang Q, Tallury SS, Qiu Y, Pasquinelli MA. Interfacial characteristics of a carbon nanotube-polyimide nanocomposite by molecular dynamics simulation. Nanotechnol Rev. 2020;9(1):136–45.

[9] Razavi R, Zare Y, Rhee KY. A model for tensile strength of polymer/carbon nanotubes nanocomposites assuming the percolation of interphase regions. Colloids Surf A. 2018;538:148–54.

[10] Zare Y, Rhee KY. Modeling of viscosity and complex modulus for poly(lactic acid)/poly(ethylene oxide)/carbon nanotubes nanocomposites assuming yield stress and network breaking time. Composites Part B. 2019;156:100–7.

[11] Wu Q, Miao W-s, Gao H-j, Hui D. Mechanical properties of nanomaterials: a review. Nanotechnol Rev. 2020;9(1):259–73.

[12] Liu Y, Jiang X, Shi J, Luo Y, Tang Y, Wu Q, et al. Research on the interface properties and strengthening–toughening mechanism of nanocarbon-toughened ceramic matrix composites. Nanotechnol Rev. 2020;9(1):190–208.

[13] Zhang Y-F, Du F-P, Chen L, Yeung K-W, Dong Y, Law W-C, et al. Supramolecular ionic polymer/carbon nanotube composite hydrogels with enhanced electromechanical performance. Nanotechnol Rev. 2020;9(1):478–88.

[14] Zare Y. The roles of nanoparticles accumulation and interphase properties in properties of polymer particulate nanocomposites by a multi-step methodology. Composites Part A. 2016;91:127–32.

[15] Zare Y, Garmabi H. Modeling of interfacial bonding between two nanofillers (montmorillonite and $CaCO_3$) and a polymer matrix (PP) in a ternary polymer nanocomposite. Appl Surf Sci. 2014;321:219–25.

[16] Zare Y, Rhee KY. Evaluation of the tensile strength in carbon nanotube-reinforced nanocomposites using the expanded Takayanagi model. JOM. 2019;71:3980–8.

[17] Ventrapragada LK, Creager SE, Rao AM, Podila R. Carbon nanotubes coated paper as current collectors for secondary Li-ion batteries. Nanotechnol Rev. 2019;8(1):18–23.

[18] Kalwar K, Shen M. Electrospun cellulose acetate nanofibers and Au@AgNPs for antimicrobial activity – a mini review. Nanotechnol Rev. 2019;8(1):246–57.

[19] Rostami A, Moosavi MI. High-performance thermoplastic polyurethane nanocomposites induced by hybrid application of functionalized graphene and carbon nanotubes. J Appl Polym Sci. 2019;137:48520.

[20] Zare Y, Park SP, Rhee KY. Analysis of complex viscosity and shear thinning behavior in poly(lactic acid)/poly(ethylene oxide)/carbon nanotubes biosensor based on Carreau–Yasuda model. Res Phys. 2019;13:102245.

[21] Zare Y, Rhee KY. Tensile strength prediction of carbon nanotube reinforced composites by expansion of cross-orthogonal skeleton structure. Composites Part B. 2019;161:601–7.

[22] Zare Y, Garmabi H, Rhee KY. Structural and phase separation characterization of poly(lactic acid)/poly(ethylene oxide)/carbon nanotube nanocomposites by rheological examinations. Composites Part B. 2018;144:1–10.

[23] Li H-x, Zare Y, Rhee KY. The percolation threshold for tensile strength of polymer/CNT nanocomposites assuming filler network and interphase regions. Mater Chem Phys. 2018;207:76–83.

[24] Zare Y. Effects of imperfect interfacial adhesion between polymer and nanoparticles on the tensile modulus of clay/polymer nanocomposites. Appl Clay Sci. 2016;129:65–70.

[25] Zare Y, Rhee KY. Simplification and development of McLachlan model for electrical conductivity of polymer carbon nanotubes nanocomposites assuming the networking of interphase regions. Composites Part B. 2019;156:64–71.

[26] Zare Y. Modeling of tensile modulus in polymer/carbon nanotubes (CNT) nanocomposites. Synth Met. 2015;202:68–72.

[27] Kalantari E, Naghib SM, Iravani NJ, Esmaeili R, Naimi-Jamal MR, Mozafari M. Biocomposites based on hydroxyapatite matrix reinforced with nanostructured monticellite ($CaMgSiO_4$) for biomedical application: synthesis, characterization, and biological studies. Mater Sci Eng C. 2019;105:109912.
[28] Kalantari E, Naghib SM. A comparative study on biological properties of novel nanostructured monticellite-based composites with hydroxyapatite bioceramic. Mater Sci Eng C. 2019;98:1087–96.
[29] Berger P, Adelman NB, Beckman KJ, Campbell DJ, Ellis AB, Lisensky GC. Preparation and properties of an aqueous ferrofluid. J Chem Educ. 1999;76(7):943–48.
[30] Glawdel T, Elbuken C, Ren CL. Droplet formation in microfluidic T-junction generators operating in the transitional regime. II. Modeling. Phys Rev E. 2012;85(1):016323.
[31] Menech MD, Garstecki P, Jousse F, Stone HA. Transition from squeezing to dripping in a microfluidic T-shaped junction. J Fluid Mech. 2008;595(1):141–61.
[32] Zare Y, Rhee KY. Effects of interphase regions and filler networks on the viscosity of PLA/PEO/carbon nanotubes biosensor. Polym Compos. 2019;40:4135–41.
[33] Naghib SM, Rabiee M, Omidinia E, Khoshkenara P, Zeini D. Biofunctionalization of dextran-based polymeric film surface through enzyme immobilization for phenylalanine determination. Int J Electrochem Sci. 2012;7(1):120–35.
[34] Morelli S, Holdich RG, Dragosavac MM. Chitosan and poly (vinyl alcohol) microparticles produced by membrane emulsification for encapsulation and pH controlled release. Chem Eng J. 2016;288:451–60.
[35] Kalkhoran AHZ, Vahidi O, Naghib SM. A new mathematical approach to predict the actual drug release from hydrogels. Eur J Pharm Sci. 2018;111:303–10.
[36] Askari E, Naghib SM, Seyfoori A, Maleki A, Rahmanian M. Ultrasonic-assisted synthesis and in vitro biological assessments of a novel herceptin-stabilized graphene using three dimensional cell spheroid. Ultrason Sonochem. 2019;58:104615.
[37] Gooneh-Farahani S, Naimi-Jamal MR, Naghib SM. Stimuli-responsive graphene-incorporated multifunctional chitosan for drug delivery applications: a review. Exp Opin Drug Del. 2019;16(1):79–99.
[38] Saberi J, Ansari M, Hoseinzadeh BE, Kordestani SS, Naghib SM. Chitosan-polyacrylic acid hybrid nanoparticles as novel tissue adhesive: synthesis and characterization. Fibers Polym. 2018;19(12):2458–64.
[39] Naghib SM, Rabiee M, Omidinia E. Electrochemical biosensor for L-phenylalanine based on a gold electrode modified with graphene oxide nanosheets and chitosan. Int J Electrochem Sci. 2014;9:2341–53.
[40] Gooneh-Farahani S, Naghib SMN, Naimi-Jamal MR. A critical comparison study on the pH-sensitive nanocomposites based on graphene-grafted chitosan for cancer theragnosis. Multidiscip Cancer Invest. 2019;3(1):5–16.
[41] Gooneh-Farahani S, Naghib SM, Naimi-Jamal MR. A novel and inexpensive method based on modified ionic gelation for pH-responsive controlled drug release of homogeneously distributed chitosan nanoparticles with a high encapsulation efficiency. Fibers Polym. 2020;21(9):1917–26.
[42] Naghib SM, Zare Y, Rhee KY. A facile and simple approach to synthesis and characterization of methacrylated graphene oxide nanostructured polyaniline nanocomposites. Nanotechnol Rev. 2020;9(1):53–60.
[43] Naghib SM, Behzad F, Rahmanian M, Zare Y, Rhee KY. A highly sensitive biosensor based on methacrylated graphene oxide-grafted polyaniline for ascorbic acid determination. Nanotechnol Rev. 2020;9(1):760–7.
[44] Zhu Z, Zhang W, Leng X, Zhang M, Guan Z, Lu J, et al. Highly sensitive and quantitative detection of rare pathogens through agarose droplet microfluidic emulsion PCR at the single-cell level. Lab Chip. 2012;12(20):3907–13.
[45] Shi B, Wu D, Jiang Y, An J, Wu W. Off-chip vertical step emulsification droplets preparation device applied for droplet digital PCR. Adv Mater Interfaces. 2020;7(22):2001074.
[46] Kung C-T, Gao H, Lee C-Y, Wang Y-N, Dong W, Ko C-H, et al. Microfluidic synthesis control technology and its application in drug delivery, bioimaging, biosensing, environmental analysis and cell analysis. Chem Eng J. 2020;399(1):125748.
[47] Wang Y, Chen Z, Bian F, Shang L, Zhu K, Zhao Y. Advances of droplet-based microfluidics in drug discovery. Expert Opin Drug Discovery. 2020;15(1):1–11.
[48] Chen Y, Li K, Zhang S, Qin L, Deng S, Ge L, et al. Bioinspired superwettable microspine chips with directional droplet transportation for biosensing. ACS Nano. 2020;14(4):4654–61.
[49] Hassanzadeh-Barforoushi A, Warkiani ME, Gallego-Ortega D, Liu G, Barber T. Capillary-assisted microfluidic biosensing platform captures single cell secretion dynamics in nanoliter compartments. Biosens Bioelectron. 2020;155:112113.
[50] Tu R, Li L, Yuan H, He R, Wang Q. Biosensor-enabled droplet microfluidic system for the rapid screening of 3-dehydroshikimic acid produced in *Escherichia coli*. J Ind Microbiol Biotechnol. 2020;1–6.
[51] Lu Z, Li Y, Qiu W, Rogach AL, Nagl S. Composite films of $CsPbBr_3$ perovskite nanocrystals in a hydrophobic fluoropolymer for temperature imaging in digital microfluidics. ACS Appl Mater Interfaces. 2020;12(17):19805–12.
[52] Alizadeh N, Ghasemi F, Salimi A, Hallaj R, Fathi F, Soleimani F. Polymer nanocomposite film for dual colorimetric and fluorescent ascorbic acid detection integrated single-cell bioimaging with droplet microfluidic platform. Dyes Pigm. 2020;173:107875.
[53] Rosenfeld L, Lin T, Derda R, Tang SK. Review and analysis of performance metrics of droplet microfluidics systems. Microfluid Nanofluid. 2014;16(5):921–39.
[54] Wang J, Shao C, Wang Y, Sun L, Zhao Y. Microfluidics for medical additive manufacturing. Engineering. 2020;6(11):1244–57.
[55] Riahi R, Tamayol A, Shaegh SAM, Ghaemmaghami AM, Dokmeci MR, Khademhosseini A. Microfluidics for advanced drug delivery systems. Curr Opin Chem Eng. 2015;7:101–12.
[56] Duncanson WJ, Lin T, Abate AR, Seiffert S, Shah RK, Weitz DA. Microfluidic synthesis of advanced microparticles for encapsulation and controlled release. Lab Chip. 2012;12(12):2135–45.
[57] Champion JA, Katare YK, Mitragotri S. Particle shape: a new design parameter for micro-and nanoscale drug delivery carriers. J Controlled Release. 2007;121(1-2):3–9.

[58] Gañán-Calvo AM, Montanero JM, Martín-Banderas L, Flores-Mosquera M. Building functional materials for health care and pharmacy from microfluidic principles and flow focusing. Adv Drug Delivery Rev. 2013;65(11–12):1447–69.
[59] Sartipzadeh O, Naghib SM, Seyfoori A, Rahmanian M, Fateminia FS. Controllable size and form of droplets in microfluidic-assisted devices: effects of channel geometry and fluid velocity on droplet size. Mater Sci Eng C. 2020;109:110606.
[60] Cristini V, Tan Y-C. Theory and numerical simulation of droplet dynamics in complex flows – a review. Lab Chip. 2004;4(4):257–64.
[61] Wang K, Lu YC, Xu JH, Luo GS. Determination of dynamic interfacial tension and its effect on droplet formation in the T-shaped microdispersion process. Langmuir. 2009;25(4):2153–8.
[62] Lee W, Walker LM, Anna SL. Role of geometry and fluid properties in droplet and thread formation processes in planar flow focusing. Phys Fluids. 2009;21(3):032103.
[63] Chen X, Glawdel T, Cui N, Ren CL. Model of droplet generation in flow focusing generators operating in the squeezing regime. Microfluid Nanofluid. 2015;18(5–6):1341–53.